CYBERNETICS AND PHYSICS, VOL. 14, NO. 4, 2025, 383–391

ENERGY-SAVING CONTROL OF GEOSTATIONARY SATELLITE DURING LONG-TERM MOTHBALLING

Yevgeny Somov
Navigation, Guidance and Control
Samara State Technical University
Samara, Russia
e_somov@mail.ru

Sergey Somov
Navigation, Guidance and Control
Samara State Technical University
Samara, Russia
s_somov@mail.ru

Sergey Butyrin
Navigation, Guidance and Control
Samara State Technical University
Samara, Russia
butyrinsa@mail.ru

Tatyana Somova
Navigation, Guidance and Control
Samara State Technical University
Samara, Russia
te_somova@mail.ru

Alexey Dobrosotskikh
Electric Power Stations
Samara State Technical University
Samara, Russia
dob_as@mail.ru

Article history:
Received 26.09.2025, Accepted 20.12.2025

Abstract

Methods for analyzing the spatial motion of a satellite in geostationary orbit during long-term conservation with episodic activation of control have been developed. The computer simulation results of a geostationary communications satellite motion during the year with quarterly correction are presented.

1 Introduction

In memory of elite Profs by the Russia and ICS RAS *V.Yu. Rutkovsky*, S.D. Zemlikov, *V.M. Sukhanov*, and V.M. Glumov in research of space robot control systems.

Currently, various countries have begun to introduce space communication systems consisting of thousands of mini-satellites in low orbits. A worthy answer of traditional space communication technology [Testoyedov et al., 2017], Fig. 1, is based on a new generation of communications satellites that are assembled in geostationary orbit (GSO) by space robot manipulators (SRMs) [Somov et al., 2019] using replaceable and replenished components, and then regularly serviced by SRMs for several decades. Modern information satellites in GSO are usually used with a guaranteed period of their target operation of up to 17 years. The main limitation of the service life for such geostationary communications satellites (GCS) is the exhaustion of fuel for the plasma electric propulsion unit (EPU) to keep a serviceable satellite in the GSO. There are two types of projects here: 1) a space robot manipulator for refueling the EPU, including by a simple replacement of fuel tanks, and its maintenance, including the GCS onboard equipment and 2) a space tug, which is mated with an existing satellite and retains it in the GSO, using its EPU.

There are already some practical results of the projects of the second type, since they are simpler. For instance, the space tug *Mission Extension Vehicle-1* (*MEV-1*) has been created by *Northrop Grumman* (USA) to extend the service life of GCS that are running out or have already run out of fuel. On February 25, 2020, the *MEV-1* tug successfully docked to the *Intelsat 901* communications satellite which operated in the GSO in 2001-2016. After having been moved, this satellite resumed its work on April 2, 2020. The *MEV-2* space tug was launched on August 15, 2020, to extend the service life of the *Intelsat 10-02* satellite, which has been operating in the GSO since June 16, 2004. Successful docking of *MEV-2* with *Intelsat 10-02* spacecraft was performed on April 12, 2021, and currently this satellite is successfully operating. The latest advances in space refueling are available in [SR, 2022; SR, 2024a; SR, 2024b; SR, 2025].

Figure 1. Geostationary communications satellite *Express*-AM5/6

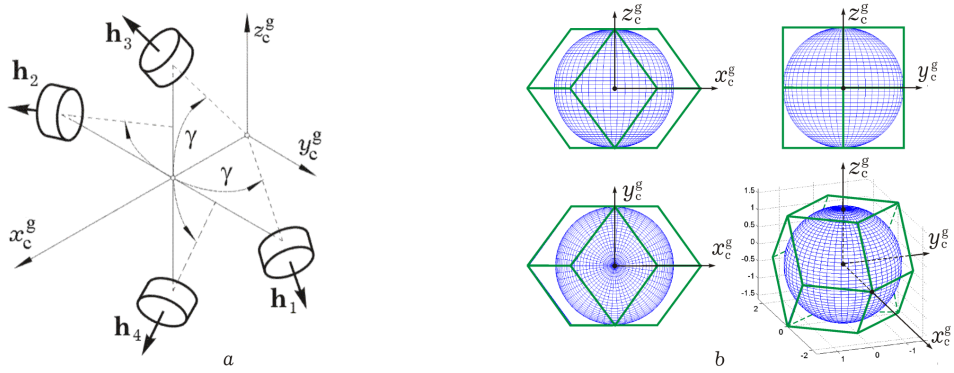

Figure 2. The GE scheme of the RW cluster (a) and its angular momentum's variation domain with optimal configuration (b)

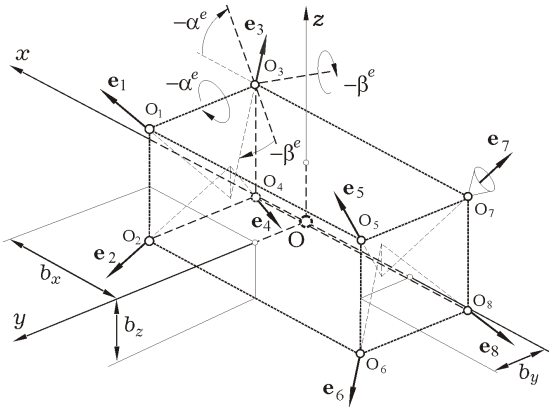

Figure 3. The scheme of EPU with eight catalytic EJEs

When refueling the EPU with the tanks being replaced, such filled fuel tanks should be delivered by a space robot within about 4 months according to a combined scheme of its launching to the vicinity of the GCS standing point. However, due to many organizational and technical risks, such launching of the SRM with fuel tanks may be delayed for several months. So, such projects provide for a GCS *conservation mode* with a duration, for example, of at least one year. It should be noted that GCS *Intelsat 901* was in the burial orbit for more than *3 years* (!) waiting for the *MEV-1* tug. Here a natural and intriguing question arises: how can this be achieved with a shortage of fuel for the EPU ?

The long-term conservation mode consists in a passive flight of the GCS, maintaining a positive average balance of its power supply and activating episodically its attitude and orbit control system (AOCS) to keep the satellite in the vicinity of a given standing point in the GSO.

In the AOCS, a cluster of flywheels – the reaction wheels (RWs) by scheme *General Electric* (*GE*) [Somov et al., 2021a], Fig. 2a, with digital control is applied, as well as two EPUs based on both plasma and catalytic electric jet engines (EJEs) [Somov et al., 2020], Fig. 3, and also an electromechanical drive of solar array panels (SAPs), see Fig. 1 with Russian GCS *Express*-AM5/6.

Curious mathematicians usually study problems of astrodynamics for a set of points with a known mass without taking into account the influence of the solar pressure force (SPF), see [Aminov et al., 2019], where only "impulse correction" of the probe's motion during long-term stay in the vicinity of Lagrange point L_1 into the Sun-Earth system is studied. The point L_1 is suited to study the system, but the probe is almost always illuminated by the Sun, that gradually leads to large accumulated force and torque vectors [Polyakhova, 2011].

This article represents developed strategy for the GCS motion control in the long-term conservation mode and extended results on computer simulation for the GCS with large-sized SAPs [Somov and Somova, 2022].

2 Main models and the problem statement

We use standard inertial reference frame (IRF) $\mathbf{I}_{\oplus}$, inertial solar-ecliptic reference frame $\mathbf{I}_{\odot}$, as well as the GCS body reference frame (BRF) $\mathbf{B}$ ($Oxyz$), the orbit reference frame (ORF) $Ox^{\mathrm{o}}y^{\mathrm{o}}z^{\mathrm{o}}$, and also the SAPs' reference frame (PRF) $Ox^{\mathrm{p}}y^{\mathrm{p}}z^{\mathrm{p}}$, Figs. 3–6. The ORF with origin O in the GCS' mass center has the following directions of axes: the axis x^{o} is directed along a radial $\mathbf{r}^{\mathrm{o}}$, the axis z^{o} is along a normal $\mathbf{n}^{\mathrm{o}}$ to the orbital plane, and the axis y^{o} with an orbit transversal $\boldsymbol{\tau}^{\mathrm{o}}$. Unit vector $\mathbf{s}$ is directed from the Earth $\oplus$ to the Sun $\odot$, and the normal $\mathbf{n}^{\mathrm{p}}$ to the SAPs' plane is directed along the PRF axis x^{p}. We use the notation $\{\cdot\} \equiv \mathrm{col}(\cdot)$, $[\cdot] \equiv \mathrm{line}(\cdot)$ for vectors with scalar $\langle\cdot,\cdot\rangle$, vector $(\{\cdot\}\times\{\cdot\})$ and dyad $[\{\cdot\}\cdot\{\cdot\}]$ products; $[\cdot\times]$, $(\cdot)^{\mathrm{t}}$, $\lceil\cdot\rfloor \equiv \mathrm{diag}(\cdot)$ for matrices and $\circ$, $\tilde{}$ for quaternions $\boldsymbol{\Lambda} = (\lambda_0, \boldsymbol{\lambda}), \boldsymbol{\lambda} = \{\lambda_1, \lambda_2, \lambda_3\}$, also $\boldsymbol{\sigma} = \mathbf{e}\tan(\Phi/4)$ for vector of modified Rodrigues parameters (MRP) with Euler unit vector $\mathbf{e}$ and angle Φ

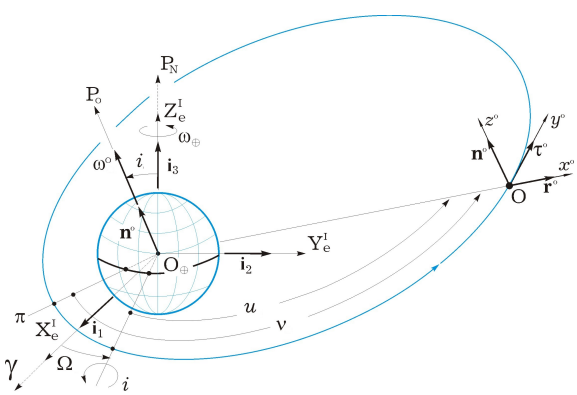

Figure 4. Basic reference frames for satellite orbital flight

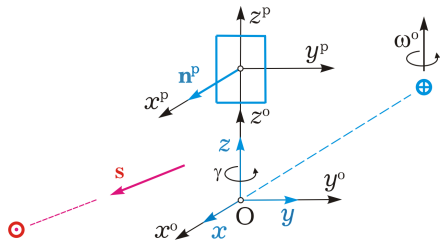

Figure 5. Reference frames in normal mode of GCS operation

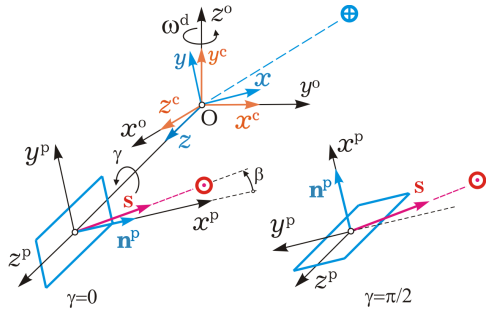

Figure 6. Reference frames in the GCS conservation mode

of own rotation, $C_\alpha = \cos\alpha$ and $S_\alpha = \sin\alpha$. The vector $\boldsymbol{\sigma}$ is connected with quaternion $\boldsymbol{\Lambda}$ by explicit relations.

The BRF has the unit vectors $\mathbf{b}_i$, $i = 1 \div 3 = x, y, z$, which are directed along its respective axes. We introduce also a *central* body reference frame (CBRF) $\mathbf{B}^c$ ($Ox^cy^cz^c$) with unit vectors $\mathbf{b}_i^c$, directed along the *main central* axes of the satellite inertia tensor $\mathbf{J} = \| J_{ij} \|$. In the CBRF, this inertia tensor has a diagonal representation $\mathbf{J}^c = \lceil J_i^c \rfloor$. In the ORF, the BRF orientation is determined by angles of yaw $\phi_1 = \psi$, roll $\phi_2 = \varphi$ and pitch $\phi_3 = \theta$ in the sequence 132, and the CBRF orientation – by angles ϕ_1^c, ϕ_2^c and ϕ_3^c in the same sequence. The GCS is considered as a solid, so with standard notation [Somov et al., 2021a; Somov et al., 2020] its spatial motion is presented in the form

$$\begin{aligned} &\dot{\mathbf{r}} = \mathbf{r}' + \boldsymbol{\omega} \times \mathbf{r}; \quad \mathrm{m}(\mathbf{v}' + \boldsymbol{\omega} \times \mathbf{v}) = \mathbf{P}^e + \mathbf{F}^d; \\ &\dot{\boldsymbol{\Lambda}} = \boldsymbol{\Lambda} \circ \boldsymbol{\omega}/2; \quad \dot{\mathbf{K}} + \boldsymbol{\omega} \times \mathbf{G} = \mathbf{M}^r + \mathbf{M}^e + \mathbf{M}^d. \end{aligned} \tag{1}$$

Here, $\mathbf{v} = \mathbf{r}' + \boldsymbol{\omega} \times \mathbf{r}$ is the velocity vector of GCS forward motion; $\mathbf{K} = \mathbf{J}\boldsymbol{\omega}$ is vector of the GCS angular momentum (AM), vector $\mathbf{G} = \mathbf{K} + \mathbf{H}$, vector $\mathbf{H} \equiv \{\mathrm{H}_i\} = \mathbf{A}_4\mathbf{h}$ represents the AM of the RW cluster; matrix $\mathbf{A}_4 = [\mathbf{a}_p]$ composed of unit vectors $\mathbf{a}_p$ by RW axes; $\mathbf{h} = \{\mathrm{h}_p\}$, $p = 1 \div 4$; the RW cluster control vector $\mathbf{M}^r = \mathbf{M} = -\mathbf{A}_4\dot{\mathbf{h}} = \mathbf{A}_4\mathbf{m}$ with $\mathbf{m} = \{\mathrm{m}_p\}$, vectors of thrust $\mathbf{P}^e$ and torque $\mathbf{M}^e$ are the EPUs controls.

At last $\mathbf{F}^d$ and $\mathbf{M}^d$ are other external force and torque vectors, including torque vectors of the SPF $\mathbf{M}^s = \{\mathrm{M}_i^s\}$ and gravity $\mathbf{M}^g = \{\mathrm{M}_i^g\}$ due to gravitational influence of the Earth, Moon and Sun.

Let be given the quaternion $\boldsymbol{\Lambda}^d$, velocity $\boldsymbol{\omega}^d$ and acceleration $\boldsymbol{\varepsilon}^d$ vectors for designed angular state of the GCS. Then the error quaternion $\mathbf{E} = (e_0, \mathbf{e}) = \tilde{\boldsymbol{\Lambda}}^d \circ \boldsymbol{\Lambda}$ with $\mathbf{e} = \{e_i\}$ corresponds to the angular error matrix $\mathbf{C}^e = \mathbf{I}_3 - 2[\mathbf{e}\times]\mathbf{Q}_e^t$ with $\mathbf{Q}_e = \mathbf{I}_3 e_0 + [\mathbf{e}\times]$, the MRP vector $\boldsymbol{\sigma}^e = \mathbf{e}^e \tan(\Phi^e/4)$ and the angular error vector $\delta\boldsymbol{\phi} = \{\delta\phi_i\} = 2\{e_0 e_i\}$. The error vector $\delta\boldsymbol{\omega} \equiv \boldsymbol{\omega}^e$ in angular velocity is calculated by the ratio $\boldsymbol{\omega}^e = \boldsymbol{\omega} - \mathbf{C}^e\boldsymbol{\omega}^d$.

In normal mode, the GCS is stabilized in ORF when electrical axes of its antennas are directed to nadir, and the normal $\mathbf{n}^p$ to the SAPs is directed to the Sun, Fig. 5.

The peculiarity of GCS design is the ratio $J_y = J_{22} > J_x = J_{11} > J_z = J_{33}$, which leads to problems of stability for the GCS angular position in the ORF. This feature also manifests itself for the satellite's main central moments of inertia, namely in the form $J_y^c > J_x^c > J_z^c$. At passive flight of the GCS, its angular motion in the ORF mainly depends on the SPF $\mathbf{M}^s$ and gravity $\mathbf{M}^g$ torque vectors. The problem is to develop a strategy for the GCS AOCS operation in the conservation mode and its testing based on computer simulation methods.

At the ICS RAS, the problems of robot control when satellites maintenance have been studied for many years by Prof. *V. Yu. Rutkovsky* team, for example [Bogomolov et al., 1998], [Rutkovsky and Sukhanov, 2000], [Glumov et al., 2001], [Glumov et al., 2006], [Zemlyakov et al., 2006], [Rutkovsky et al., 2010a; Rutkovsky et al., 2010b; Rutkovsky et al., 2010c], [Rutkovsky et al., 2011], [Rutkovsky et al., 2013], [Sukhanov et al., 2014], [Rutkovsky et al., 2015], [Sukhanov et al., 2015], [Glumov et al., 2018], [Rutkovsky and Glumov, 2023]. Research and developments on this topic are being carried out in many Russian universities: [Alpatov et al., 2010], [Timofeev and Shardyko, 2013], [Alpatov et al., 2013], [Dalyaev et al., 2015], [Belonozhko, 2015], [Belonozhko, 2019], [Katkalov, 2020a], [Katkalov, 2020b], [Katkalov and Morozova, 2022].

3 Conservation strategy

The developed strategy is based on the following sequentially performed actions.

1. When the GCS standard orientation in the ORF, bringing the SAPs to the park position with angle $\gamma = 0$, see Fig. 5. The angular velocity vector $\boldsymbol{\omega}^o$ of the GCS orbital motion is defined in the form $\boldsymbol{\omega}^o = \omega^o\mathbf{n}^o$.

2. The GCS body reversal in the ORF to the position when unit vector $\mathbf{b}_2^c$ with maximum central moment of inertia J_y^c is directed along the normal $\mathbf{n}^o$, and the unit vector $\mathbf{b}_3^c$ with minimum central moment of inertia J_z^c – along the radial $\mathbf{r}^o$, see Fig. 6. That reversal is performed using the RW cluster and onboard digital reference guidance model for the MRP vector [Somov et al., 2021a].

3. Acceleration of the GCS body rotation around the axis Oy^c located near the normal $\mathbf{n}^o$. Such acceleration to a given rotation velocity $\omega^d = 24\omega^o$ (Fig. 6) with subsequent stabilization is performed by the RW cluster.

4. Braking of the RWs and stabilization of the GCS body rotation by the EPU based on 8 catalytic EJEs with pulse-width modulation (PWM) of their thrust.

5. The AOCS shutdown and subsequent flight of GCS, stabilized by rotation [Artyukhin et al., 1979; Popov, 1986], at a time interval lasting up to 3 months. Such

intervals can be repeated with the AOCS short-term inclusion to correct the orbit of the GCS and return its location to the vicinity of a given standing point on GSO.

Over the past 50 years, many monographs and textbooks have been published on the research and design of the spacecraft AOCS [Elyasberg, 1965; Rauschenbakh and Tokar, 1974; Smirnov et al., 1985; Battin, 1999; Wie, 2008; Schaub and Junkins, 2009; Vallado, 2013; Markley and Crassidis, 2014; Baranov, 2016; Curtis, 2020; Montenbruck and Gill, 2020] et al. as well as review articles, for example [Somov, 2016]. So, here we briefly represent control laws of redundant drive clusters (Figs. 2 & 3) for the GCS long-term conservation and focus on the discussion of computer simulation results.

4 Redundant drive clusters and control laws

4.1 Optimizing the RW cluster configuration

For RW scheme *GE* with $a = C_\gamma, b = S_\gamma$, the unit vectors $\mathbf{a}_p$ have the form $\mathbf{a}_1 = \{a, b, 0\}$; $\mathbf{a}_2 = \{a, -b, 0\}$; $\mathbf{a}_3 = \{a, 0, b\}$; $\mathbf{a}_4 = \{a, 0, -b\}$ (Fig. 2*a*), what defines a matrix $\mathbf{A}_4 = [\mathbf{a}_p] \equiv \mathbf{A}$. We introduce normalized AM vectors $\mathbf{h}_p = h_p \mathbf{a}_p$ with limited modules $|\mathbf{h}_p| = h_p = \mathrm{h}_p/\mathrm{h}^\mathrm{m} \le 1$, a column of normalized AM by individual RWs $\mathbf{h} = \{h_p\}$ and a column of the RW cluster normalized AM $\mathbf{H} = \Sigma \mathbf{h}_p = \{x, y, z\}$, which are related by the relation $\mathbf{H} = \mathbf{A}\mathbf{h}$.

As is known [Gantmakher, 1988], a system of vectors $\mathbf{x}_p$, $p = 1 \div m$ in the Euclidean space $\mathbb{R}^m$ is linearly independent if the Gram matrix $\mathbf{G}$ composed of these vectors has a determinant $\mathsf{G} \equiv \det \mathbf{G} > 0$, which value is equal to a volume square of a m-dimensional parallelepiped created on vectors $\mathbf{a}_p$ directed along its edges.

In the analyzed RW cluster we have $m = 4$, $\mathbf{x}_p = \mathbf{a}_p$, the Gram matrix $\mathbf{G} = \mathbf{A}_4 \mathbf{A}_4^\mathrm{t} = \lceil 4a^2, 2b^2, 2b^2 \rfloor$ with determinant $\mathsf{G} = 16\, a^2 b^4 = 16\, C_\gamma^2 S_\gamma^4$. The choice of angle γ is based on maximizing the parallelepiped volume, the relations were obtained [Somov and Somova, 2021]: $d\,\mathsf{G}/d\gamma = 32 S_\gamma C_\gamma S_\gamma^2 [-S_\gamma^2 + 2C_\gamma^2] = 0 \Rightarrow \tan\gamma = \sqrt{2}$; $C_\gamma \equiv a = \sqrt{(1/3)}, S\gamma \equiv b = \sqrt{(2/3)} \Rightarrow \gamma = 54°44'$.

Let the canonical reference frame $\mathrm{O}x_\mathrm{c}^\mathrm{g} y_\mathrm{c}^\mathrm{g} z_\mathrm{c}^\mathrm{g}$ (Fig. 2) coincide with the BRF $\mathrm{O}xyz$. Then for this RW cluster in optimal configuration, the variation domain of normalized AM vector is represented in the BRF by a parallelepiped with $m(m-1) = 12$ faces, each face of which is a rhombus, Fig. 2*b*, green color. A sphere of normalized radius $r_\mathrm{h} = 2S_\gamma = 2\sqrt{(2/3)} = 1.633$, is inscribed in the AM domain and touches all 12 faces, see Fig. 2*b*.

4.2 Distribution of the RW cluster controls

The RW cluster normalized AM has the explicit form $\mathbf{H} = \{x, y, z\} = \{x_1 + x_2, b\, h_{12}^-, b\, h_{34}^-\}$ with $x_1 = a\, h_{12}^+$, $x_2 = a\, h_{34}^+$ and $h_{12}^\pm = h_1 \pm h_2$, $h_{34}^\pm = h_3 \pm h_4$. Here, the fundamental problem is a distribution of its AM $\mathbf{H} = \mathbf{A}\mathbf{h}$ and control torque (CT) $\mathbf{M} = -\mathbf{A}\mathbf{m}$ vectors between four RWs when $\mathbf{H}, \mathbf{M} \in \mathbb{R}^3$ & $\mathbf{h}, \mathbf{m} \in \mathbb{R}^4$, which consists in solving two redundant vector equations $\mathbf{A}\mathbf{h} = \mathbf{H}$ and $\mathbf{A}\mathbf{m} = -\mathbf{M}$ to obtain the columns $\mathbf{h}$ and $\mathbf{m}$ values.

In this cluster with its minimum coercion, the distribution of the AM and CT vectors is based on using of pseudo-inverse matrix $\mathbf{A}^\# = \mathbf{A}^\mathrm{t}(\mathbf{A}\mathbf{A}^\mathrm{t})^{-1}$ [Albert, 1972]; [Gantmakher, 1988]. However, here there is no uniqueness of the solution to considered problem, which leads to an accumulation of errors [Albert, 1972].

Main idea of the employed explicit distribution law consists in achieving the strict uniformity in terms of the saturation resources for the first and second RW pairs [Somova, 2016; Somov et al., 2021a]. In normalized form, the law is described by analytic relations

$$f_\rho(\mathbf{h}) = \tilde{x}_1 - \tilde{x}_2 + \rho(\tilde{x}_1 \tilde{x}_2 - 1) = 0; \qquad (2)$$

$\dot{f}_\rho(\mathbf{h}) = \langle \mathbf{a}^\mathrm{f}(\mathbf{h}), \dot{\mathbf{h}} \rangle = \Phi_\rho(f_\rho(\mathbf{h})) \equiv -\mathrm{sat}(\mu_\rho f_\rho(\mathbf{h}), \phi_\rho)$, $\tilde{x}_1 \equiv x_1/q_y$; $\tilde{x}_2 \equiv x_2/q_z$; $q_s = (a^2 - s^2)^{1/2}$, $s = y, z$; $0 < \rho < 1$; ϕ_ρ, μ_ρ and ρ are positive parameters, and column $\mathbf{a}^\mathrm{f}(\mathbf{h}) = \{a_p^\mathrm{f}\} = \partial f_\rho(\mathbf{h})/\partial\, \mathbf{h}$ has components

$$a_{1,2}^\mathrm{f} = 2a(2a^2 \pm b^2 h_2 h_{12}^-)(1 + \rho a h_{34}^+/q_z)/q_y^3;$$
$$a_{3,4}^\mathrm{f} = 2a(2a^2 \mp b^2 h_4 h_{34}^-)(1 + \rho a h_{12}^+/q_y)/q_z^3.$$

With notation $q_{yz}^\pm \equiv q_y \pm q_z$, $b_q \equiv x/2$, $c_q \equiv q_y q_z - b_q^2$ the normed AM vector $\mathbf{H} = \{x, y, z\}$ is distributed as per condition $f_\rho(\mathbf{h}) = 0$ (2) firstly among RW pairs by the relation $x_1 = (x + \Delta)/2$, $x_2 = (x - \Delta)/2$, where

$$\Delta \equiv (q_{yz}^+/\rho)(1 - (1 - 4\rho[q_{yz}^- b_q + \rho\, c_q]/(q_{yz}^+)^2)^{1/2}),$$

and next among two RWs in each pair by evident relations. To define column $\mathbf{m}$, the relation $\mathbf{A}\dot{\mathbf{h}} = \dot{\mathbf{H}}$ is supplemented with equation $\langle \mathbf{a}^\mathrm{f}(\mathbf{h}), \dot{\mathbf{h}} \rangle = \Phi_\rho(f_\rho(\mathbf{h}))$.

As a result, we obtain four linear equations and the column $\mathbf{m} = \{\mathsf{m}_p\}$ of the RW cluster control torques is calculated as $\mathbf{m} = \{\mathbf{A}, [\mathbf{a}_p^\mathrm{f}]\}^{-1}\{-\mathbf{M}^\mathrm{r}, \mathrm{h}^\mathrm{m}\Phi_\rho(f_\rho(\mathbf{h}))\}$.

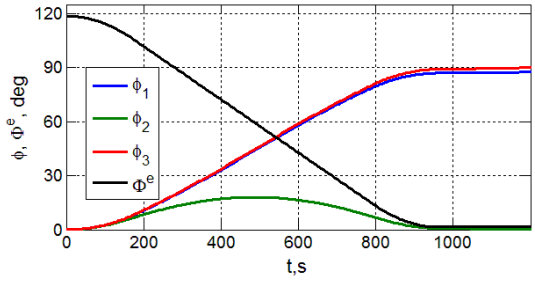

Figure 7. Changing the GCS orientation angles in the ORF

4.3 Distribution of catalytic EJE cluster controls

In the EPU with 8 catalytic EJEs (Fig. 3) we represent the unit vectors $\mathbf{e}_p$,$p = 1 \div 8$ of the EJE nozzle axes. Assume that vector $\boldsymbol{\rho}_p \in \{\pm b_x, \pm b_y, \pm b_z\}$ defines the point O_p at which the thrust vector of the p-th EJE is applied. Each catalytic EJE has the PWM of its thrust $p_p(t)$, which is described by the nonlinear relations $p_p(t) = \mathrm{P}^\mathrm{m}\,\mathrm{PWM}(t - T_{zu}^\mathrm{e}, t_r, \tau_m, \mathrm{v}_{p\,r})\ \forall t \in [t_r, t_{r+1})$, $t_{r+1} = t_r + T_u^\mathrm{e}$, $r \in \mathbb{N}_0 \equiv [0, 1, 2, \dots)$ with a period T_u^e and a time delay T_{zu}^e. Here P^m is the nominal value of a thrust, similar for all catalytic EJEs, and the function

$$\mathrm{PWM}(t, t_r, \tau_m, \mathrm{v}_{pr}) \equiv \begin{cases} \mathrm{sign}\,\mathrm{v}_{pr} & t \in [t_r, t_r + \tau_{pr}), \\ 0 & t \in [t_r + \tau_{pr}, t_{r+1}); \end{cases}$$

$$\tau_{p\,r} \equiv \begin{cases} 0 & |\mathrm{v}_{pr}| \le \tau_m, \\ \mathrm{sat}\,(T_u^\mathrm{e},\ |\mathrm{v}_{pr}|) & |\mathrm{v}_{pr}| > \tau_m. \end{cases}$$

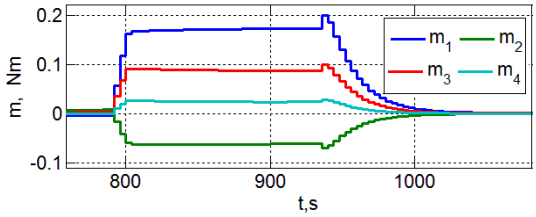

Figure 8. The RW control torques at the end of the GCS reversal

The thrust vector of p-th EJE is calculated by relation $\mathbf{p}_p(t) \equiv \{\mathrm{p}_p\} = -p_p(t)\,\mathbf{e}_p$, and vectors of the EPU force $\mathbf{P}^{\mathrm{e}} \equiv \mathbf{P} = \{\mathrm{P}_i\}$ and torque $\mathbf{M}^{\mathrm{e}}$ are computed by the formulas $\mathbf{P}^{\mathrm{e}} = \Sigma\,\mathbf{p}_p(t)$ and $\mathbf{M}^{\mathrm{e}} = \Sigma\,[\boldsymbol{\rho}_p\times]\mathbf{p}_p(t)$.

At first the command vector $\mathbf{P}^{ep}_r$ for thrust *pulse* is calculated over $t \in [t_r, t_{r+1})$ as well as the durations τ_{pr} of the PWM thrust activation for all eight EJEs are computed by explicit relations [Somov, 2017]. Here the question naturally arises: how is it possible to generate the vectors $\mathbf{P}^{ep}$ and $\mathbf{M}^{ep}$ with arbitrary direction in the BRF if the EJE nozzle axes are fixed and each EJE may be only in two states – it is switched on or switched off ?

To solve this problem, we have applied the PWM trust of all eight EJEs, that modulation ensures given values of vector $\mathbf{P}^{ep}_r \equiv \mathbf{P}^{ep}(t_r)$. We use the notation $\mathbf{r}_p = \boldsymbol{\rho}_p/\rho$, $\boldsymbol{\tau} = \{\tau_p\}$; $\mathbf{D}^{\mathrm{e}} = \{[\mathbf{e}_p], [\mathbf{r}_p \times \mathbf{e}_p]\}$; $\tilde{\mathbf{r}}^p = \mathbf{P}^{ep}/\mathrm{P}^{\mathrm{m}}$; $\tilde{\mathbf{m}}^p = \mathbf{M}^{ep}/(\mathrm{P}^{\mathrm{m}}\rho)$ and $\mathbf{t}^p = \{\tilde{\mathbf{r}}^p, \tilde{\mathbf{m}}^p\}$, where $\mathbf{P}^{ep}$ and $\mathbf{M}^{ep}$ are given *pulses* of the EPU force and torque vectors. Here the main problem is to solve the equation $\mathbf{D}^{\mathrm{e}}\,\boldsymbol{\tau} = \mathbf{t}^p$ for columns $\boldsymbol{\tau} \in \mathbb{R}^8_+$, $\mathbf{t}^p \in \mathbb{R}^6$ at condition that $0 \le \tau_p \le T^{\mathrm{e}}_u\ \forall p = 1 \div 8$ with respect to the components of column $\boldsymbol{\tau} = \{\tau_p\}$ when rectangular matrix $\mathbf{D}^{\mathrm{e}}$ and column $\mathbf{t}^p \in \mathbb{R}^6$ are given. For distribution of the thrust durations τ_p between eight EJEs on each time semi-interval $t \in [t_r, t_{r+1})$ we use the pseudo-inverse matrix $(\mathbf{D}^{\mathrm{e}})^{\#} \equiv (\mathbf{D}^{\mathrm{e}})^{\mathrm{t}}((\mathbf{D}^{\mathrm{e}})(\mathbf{D}^{\mathrm{e}})^{\mathrm{t}})^{-1}$. As a result, the EPU control law $\forall r \in \mathbb{N}_0$ with PWM of the EJE thrust has the following simple algorithmic form [Somov, 2017; Somov et al., 2017; Somov et al., 2022]:

$$\hat{\boldsymbol{\tau}}_r \equiv \{\hat{\tau}_{pr}\} = (\mathbf{D}^{\mathrm{e}})^{\#}\,\mathbf{t}^p_r;\quad \tilde{\tau}_{pr} =: \hat{\tau}_{pr} - \min(\hat{\tau}_{pr});$$
$$if\ \ \max(\tilde{\tau}_{pr}) > T^{\mathrm{e}}_u\ \ then\ \ \tau_{pr} = \tilde{\tau}_{pr}T^{\mathrm{e}}_u/\max(\tilde{\tau}_{pr});$$
$$\mathbf{P}^{\mathrm{e}}_r = \mathrm{P}^{\mathrm{m}}\,\tilde{\mathbf{r}}_r;\quad \mathbf{M}^{\mathrm{e}}_r = (\mathrm{P}^{\mathrm{m}}\,\rho)\,\tilde{\mathbf{m}}_r.$$

4.4 The GCS attitude guidance and control laws

When the GCS with RW cluster is considered as a free solid and the AOCS has a balance by total AM vector ($\mathbf{G} \equiv \mathbf{0}$), its angular motion in the IRF is described by kinematic model $\dot{\boldsymbol{\Lambda}} = \boldsymbol{\Lambda} \circ \boldsymbol{\omega}/2$; $\dot{\boldsymbol{\omega}} = \boldsymbol{\varepsilon} \equiv \mathbf{u} = \mathbf{J}^{-1}\mathbf{M}^{\mathrm{r}}$.

At applying the MPR vector $\boldsymbol{\sigma}$ this kinematic model of the GCS angular motion takes the form

$$\dot{\boldsymbol{\sigma}} = (1-\sigma^2)\boldsymbol{\omega}/4 + (\boldsymbol{\sigma}\times\boldsymbol{\omega} + \boldsymbol{\sigma}\,\langle\boldsymbol{\sigma},\boldsymbol{\omega}\rangle)/2;\ \dot{\boldsymbol{\omega}} = \mathbf{u} \quad (3)$$

with initial conditions $\boldsymbol{\sigma}(t_{\mathrm{o}}) = \boldsymbol{\sigma}_{\mathrm{o}}$, $\boldsymbol{\omega}(t_{\mathrm{o}}) = \boldsymbol{\omega}_{\mathrm{o}}$ and the vector $\boldsymbol{\sigma}_{\mathrm{o}} \equiv \mathbf{e}_{\mathrm{o}}\,\mathrm{tg}(\Phi_{\mathrm{o}}/4)$ is arbitrary when $|\Phi_{\mathrm{o}}| < 2\pi$.

Direct and inverse kinematic equations with the MRP vector $\boldsymbol{\sigma}$ are represented in the form $\dot{\boldsymbol{\sigma}} = \mathbf{B}(\boldsymbol{\sigma})\boldsymbol{\omega}$ and $\boldsymbol{\omega} = \mathbf{D}(\boldsymbol{\sigma})\dot{\boldsymbol{\sigma}}$ with the matrices [Somov et al., 2021a]

$$\mathbf{B}(\boldsymbol{\sigma}) \equiv \tfrac{1}{4}(1-\sigma^2)\mathbf{I}_3 + \tfrac{1}{2}([\boldsymbol{\sigma}\times] + [\boldsymbol{\sigma}\cdot\boldsymbol{\sigma}]);$$
$$\mathbf{D}(\boldsymbol{\sigma}) \equiv \mathbf{B}^{-1}(\boldsymbol{\sigma}) = (16/(1+\sigma^2)^2)\mathbf{B}^{\mathrm{t}}(\boldsymbol{\sigma}).$$

Compact notation of second derivative of function $\boldsymbol{\sigma}$ brings the controlled part of the reference guidance model to the form $\ddot{\boldsymbol{\sigma}} = \mathbf{v} \equiv \mathbf{b}(\boldsymbol{\sigma},\boldsymbol{\omega}) + \mathbf{B}(\boldsymbol{\sigma})\mathbf{u}$ with function $\mathbf{b}(\boldsymbol{\sigma},\boldsymbol{\omega}) = ([(\mathbf{B}(\boldsymbol{\sigma})\boldsymbol{\omega})\times] + [\boldsymbol{\sigma}\cdot\mathbf{B}(\boldsymbol{\sigma})\boldsymbol{\omega}])\boldsymbol{\omega}/2$.

Using the methods of feedback linearization, modal synthesis and vector Lyapunov functions [Somov, 1996] for model $\ddot{\boldsymbol{\sigma}} = \mathbf{v}$ on desired spectrum $S_* = -\alpha \pm j\beta$ we have obtained the control law $\mathbf{v} = -(k_\sigma\boldsymbol{\sigma} + k_\omega\mathbf{B}(\boldsymbol{\sigma})\boldsymbol{\omega})$.

In discrete form with period T_u and $k \in \mathbb{N}_0$ this control law is represented as $\mathbf{v}_k = -(k^d_\sigma\boldsymbol{\sigma}_k + k^d_\omega\mathbf{B}(\boldsymbol{\sigma}_k)\boldsymbol{\omega}_k)$. Here, for a given normalized regulation time T_r, the coefficients k^d_σ and k^d_ω are calculated using the relations

$$\omega_* = 3/(\xi T_r);\ \alpha = \xi\omega_*,\ \beta = \omega_*(1-\xi^2)^{1/2};$$
$$a_1 = -2\exp(-\alpha T_u)\cos(\beta T_u),\ a_2 = \exp(-2\alpha T_u);$$
$$k^d_\sigma = (1+a_1+a_2)/T^2_u,\ k^d_\omega = (3+a_1-a_2)/(2T_u),$$

which are fair $\forall\ \xi > 0$. Preliminary control law is defined as $\tilde{\mathbf{u}}(\boldsymbol{\sigma},\boldsymbol{\omega}) \equiv \{\tilde{u}_{ik}\} = \mathbf{D}(\boldsymbol{\sigma})(\mathbf{v} - \mathbf{b}(\boldsymbol{\sigma},\boldsymbol{\omega}))$, that provides uniform asymptotic stability of trivial solution for model (3), and its discrete values are represented as

$$\tilde{\mathbf{u}}_k = -[\mathbf{D}(\boldsymbol{\sigma}_k)(k^d_\sigma\boldsymbol{\sigma}_k + \mathbf{b}(\boldsymbol{\sigma}_k,\boldsymbol{\omega}_k)) + k^d_\omega\boldsymbol{\omega}_k]. \quad (4)$$

When digital control is finally formed at the time t_k, the restrictions on control vector module ($|\mathbf{u}| \equiv u \le \mathrm{u}^{\mathrm{m}}$) and angular velocity vector module ($|\boldsymbol{\omega}| \equiv \omega \le \omega^{\mathrm{m}}$) are taken into account in (4) according to the simple algorithm A: 1) by a value of digital control $\tilde{\mathbf{u}}_k$ (4) there is calculated predictive value of vector $\boldsymbol{\omega}^q_k = \boldsymbol{\omega}_k + \tilde{\mathbf{u}}_k T_u$ achieved at the end of the time interval duration T_u, and if $|\boldsymbol{\omega}^q_k| > \omega^{\mathrm{m}}$ then control vector $\tilde{\mathbf{u}}_k$ is redefined as $\tilde{\mathbf{u}}_k = (\omega^{\mathrm{m}}(\boldsymbol{\omega}^q_k/\omega^q_k) - \boldsymbol{\omega}_k)/T_u$; 2) next, if $|\tilde{\mathbf{u}}_k| \equiv \tilde{u}_k > \mathrm{u}^{\mathrm{m}}$ then vector $\mathbf{u}_k = \mathrm{u}^{\mathrm{m}}\,\tilde{\mathbf{u}}_k/\tilde{u}_k\ \forall t \in [t_k, t_{k+1})$ is formed.

The laws for the GCS digital attitude control is based on analytical relations using measured coordinates of its angular movement, details are represented in [Somov et al., 2021a; Somov et al., 2021b].

5 Computer simulation results

Computer simulation of the SPF torques was performed according to known analytical ratios, taking into account differences in the values of the reflection and absorption coefficients of the luminous flux for different sides of the SAPs. Figure 7 shows the changes in the angles of yaw, roll and pitch, as well as the angle Φ^{e} during the GCS reversal $\forall t \in [0, 940)$ s into its stable position, and Fig. 8 – the control torques of all four RWs at the end of this reversal. Next there are the important stages:
(i) $\forall t \in [940, 2944)$ s – the GCS stabilization in a stable position, balancing the SPF influence, Figs. 9 and 10;
(ii) $\forall t \in [2944, 3944)$ s – acceleration of the GCS rotation using the RW cluster to the value $\omega^{\mathrm{d}} = 24\omega^{\mathrm{o}}$ of the GCS angular velocity with subsequent its stabilization;
(iii) $\forall t \in [3944, 4944)$ s – resetting the AM vector value of the RW cluster using the catalytic EPU;
(iv) $\forall t \in [4944, 8444]$ s – stabilizing a given GCS angular rate, stop of the RWs rotation due to natural torques of dry friction; switching off the AOCS at $t = 8444$ s.

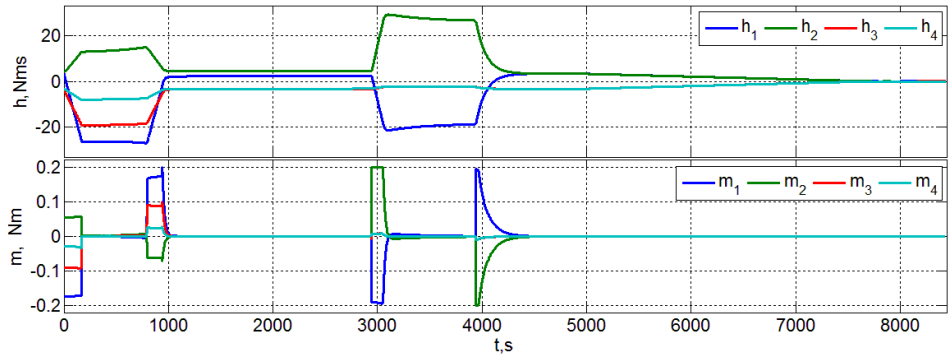

Figure 9. The AMs and CTs of flywheels during the GCS reversal, acceleration and stabilization of its rotation

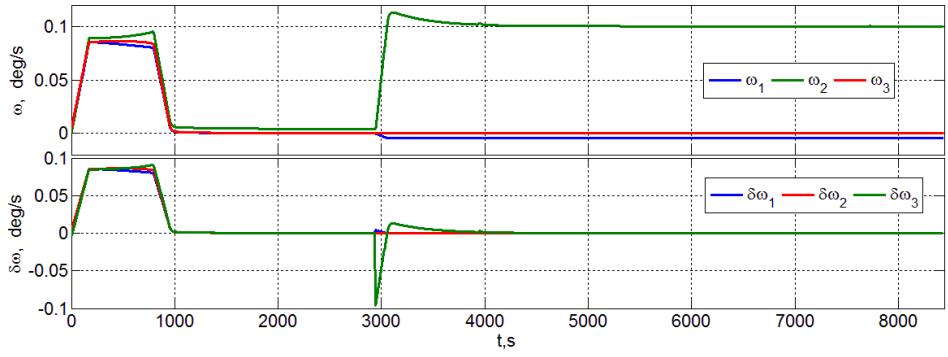

Figure 10. Angular velocity vectors $\boldsymbol{\omega}$ and $\delta\boldsymbol{\omega}$ when turning, accelerating and stabilizing the GCS rotation

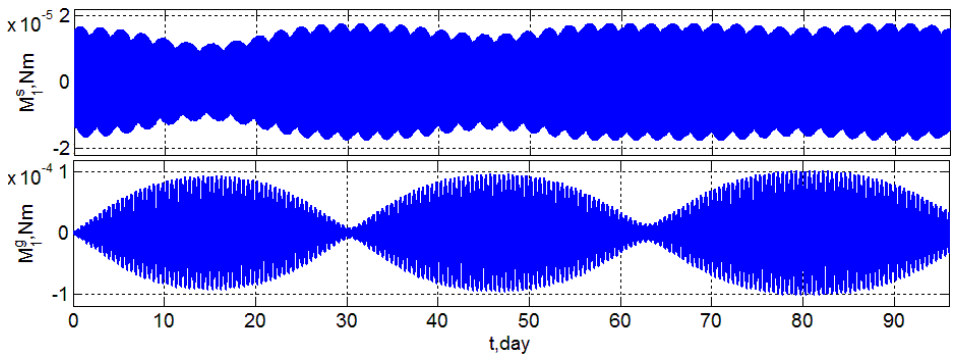

Figure 11. Change of external disturbing torques along axis Ox of the satellite BRF during 3 months

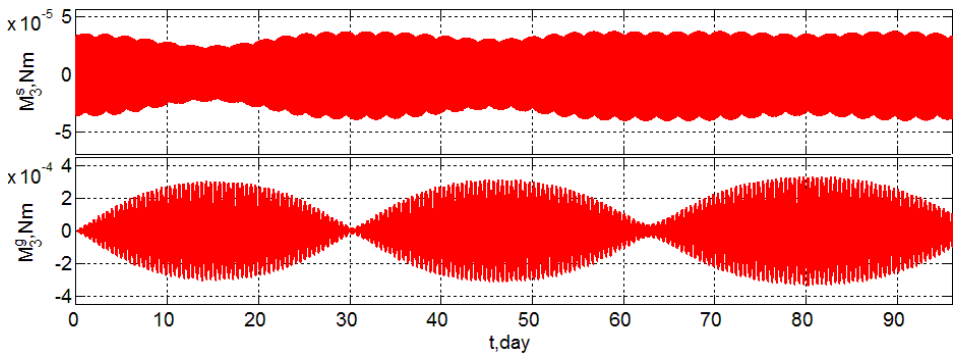

Figure 12. Change of external disturbing torques along axis Oz of the satellite BRF during 3 months

We have studied the dynamic processes of the GCS conservation in all four seasonal sections of its passive flight lasting 96 days each, namely $\pm$ 48 days relative to the centers of these sections on well-known special dates: spring equinox and summer solstice, autumn equinox and winter solstice. Figures 11–14 represent some results of the GCS passive movement during "Spring" section with a duration of 96 days starting from February 4. For example, Fig. 14 shows angular deviations of the GCS from a given position in the ORF along

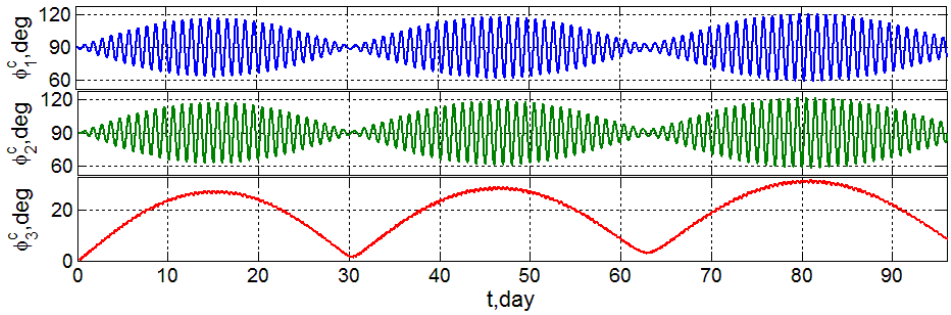

Figure 13. Changing the angles of CBRF orientation in the orbital reference frame during 3 months

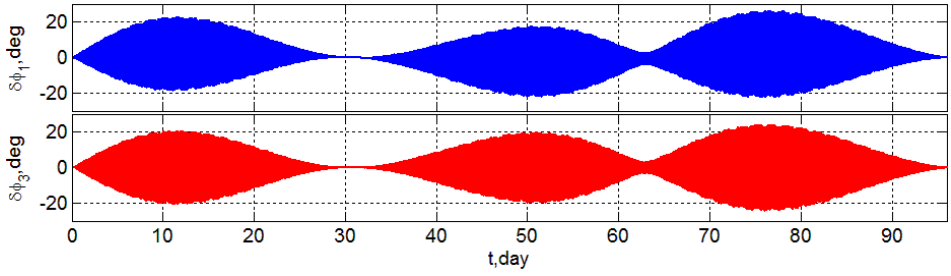

Figure 14. Angular deviations of the GCS from a given position in the ORF along the transverse axes

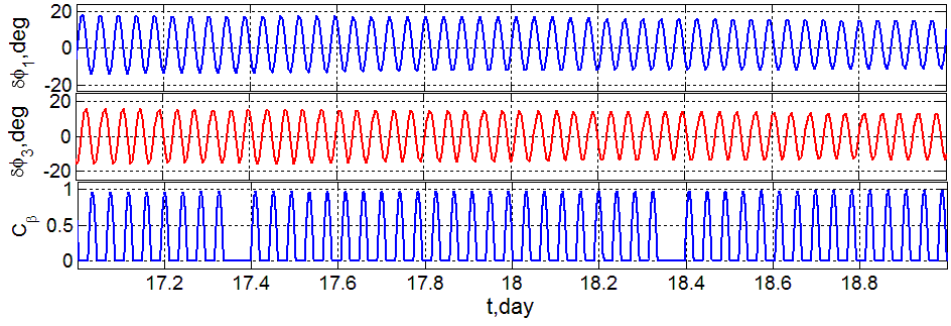

Figure 15. Changing the GCS orientation along the transverse axes and values of cos β within two days

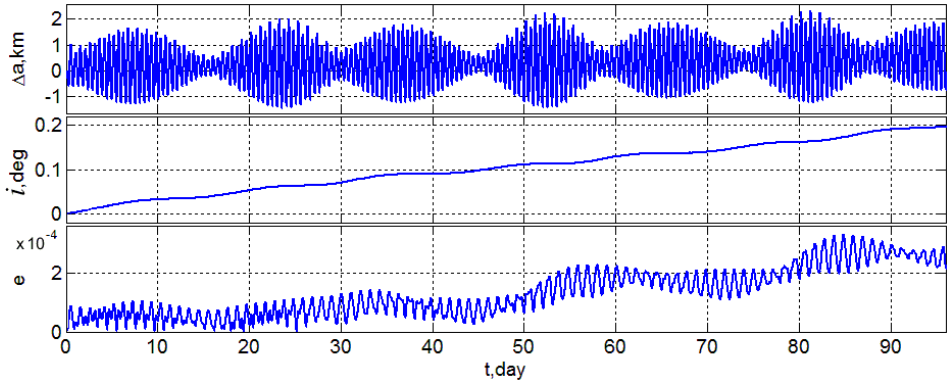

Figure 16. Changes in the semi-major axis, inclination and eccentricity of the geosynchronous orbit over 3 months

the transverse axes. On other scale, changes in these angles within two days are shown in Fig. 15, where an information is also represented on a change in values $\cos\beta$, which determines the efficiency of power supply system. Calculations have shown that in the "Spring" section with a duration of 96 days, the average $\cos\beta$ value is 0.307. Figure 16 shows the changes in the GCS orbit parameters, here it is clearly seen that with increasing time, the change in the orbit inclination increases almost monotonously. It is this circumstance that explains the appointment of 4 seasonal sections of the GCS passive flight with a duration of 96 days.

6 Conclusions

A strategy has been developed for controlling the spatial motion of a geostationary communications satellite in a long-term conservation mode, with only episodic activation of the satellite attitude and orbit control system.

The novelty of this strategy is to accelerate and stabilize the rotation of the satellite around the main central axis with the greatest moment of inertia using a cluster of four flywheels, and then in a passive gravity-stable flight of the rotating satellite lasting up to three months.

The most important new idea proposed is the digital control of the light flux reflection and absorption coefficients for given parts of the main area solar panels. This capability allows to in-flight balancing the total effect of torques due to both the gravity and solar pressure forces, see Figs. 11 and 12.

Some results of computer simulation of such conservation of a communications satellite with large-sized solar panels are briefly represented.

References

Albert, A. (1972). *Regression and the Moore-Penrose Pseudoinverse*. Academic Press, New York.

Alpatov, A. et al. (2010). Features of control system synthesis for space manipulator. *Actual Problems of Aviation & Aerospace Systems*, **15** (2(31)), pp. 38–57.

Alpatov, A. et al. (2013). Modeling the dynamics of space manipulators on a moving platform. *Robotics and Technical Cybernetics*, (1), pp. 59–65.

Aminov, R. et al. (2019). Impulse control flight to the invariant manifold near collinear libration point. *Cybernetics and Physics*, **8** (2), pp. 51–57.

Artyukhin, Y. et al. (1979). *Control Systems of Spacecraft Stabilized by Rotation*. Nauka, Moscow.

Baranov, A. (2016). *Maneuvering Spacecraft in the Vicinity of a Circular Orbit*. Sputnik +, Moscow.

Battin, R. (1999). *An Introduction to the Mathematics and Methods of Astrodynamics*. AIAA, Reston.

Belonozhko, P. (2015). Promising assembly and service robotic space modules. *Robotics and Technical Cybernetics*, (2(7)), pp. 18–23.

Belonozhko, P. (2019). Space robotics for assembly and maintenance. Potential tasks and concepts of advanced systems. *Air and Space Sphere*, (2(99)), pp. 84–97.

Bogomolov, V., Rutkovsky, V., and Sukhanov, V. (1998). Designing the optimal mechanical structure of a free-flying space robotic module as a plant at automatic control. I, II. *Automation and Remote Control*, **59** (5; 6), pp. 632–642; 814–824.

Curtis, H. (2020). *Orbital Mechanics for Engineering Students*. Elsevier, Waltham: Massachusetts.

Dalyaev, I. et al. (2015). Prospects for the creation of robotic service satellites for technical maintenance and extension of the spacecraft active service life. *Robotics and Technical Cybernetics*, (3), pp. 27–31.

Elyasberg, P. (1965). *Introduction to the Theory of Flight of Artificial Earth Satellites*. Nauka, Moscow.

Gantmakher, F. (1988). *Theory of Matrices*. Nauka, Moscow.

Glumov, V., Krutova, I., and Sukhanov, V. (2018). Some features of powered gyro stabilization of a large space structure assembled in orbit. *Automation and Remote Control*, **79** (3), pp. 524–534.

Glumov, V., Zemlyakov, S., et al. (2001). Technical controllability of the free-flying automated space module. *Automation and Remote Control*, **62** (3), pp. 370–382.

Glumov, V., Zemlyakov, S., et al. (2006). Computer-aided on-line development and derivation of the motion equation of space module. *Automation and Remote Control*, **67** (1), pp. 78–104.

Katkalov, V. (2020a). Space services and operations: state and prospects. *Air and Space Sphere*, (2), pp. 72–80.

Katkalov, V. (2020b). Prospects for the development of satellite services. *Intellectual Technologies at Transport*, (1), pp. 24–31.

Katkalov, V. and Morozova, M. (2022). Served space: new achievements and perspectives. *Spacecraft and Technologies*, (3(41)), pp. 206–217.

Markley, F. and Crassidis, J. (2014). *Fundamentals of Spacecraft Attitude Determination and Control*. Springer, New York.

Montenbruck, O. and Gill, E. (2020). *Satellite Orbits: Models, Methods, and Applications*. Springer, Berlin.

Polyakhova, E. (2011). *Space Flight with a Solar Sail: Problems and Prospects*. Librocom, Moscow.

Popov, V. (1986). *Spacecraft Orientation and Stabilization Systems*. Mashinostroyeniye, Moscow.

Rauschenbakh, B. and Tokar, E. (1974). *Spacecraft Attitude Control*. Nauka, Moscow.

Rutkovsky, V. and Glumov, V. (2023). Control of a free-flying space manipulation robot with a payload. *Automation and Remote Control*, **84** (10), pp. 1079–1087.

Rutkovsky, V. and Sukhanov, V. (2000). A dynamic model of a free-flying space robot engineering module. *Automation and Remote Control*, **61** (5), pp. 749–767.

Rutkovsky, V., Sukhanov, V., and Glumov, V. (2010a). Control of multimode manipulative space robot in outer space. *Automation and Remote Control*, **71** (11), pp. 2345–2359.

Rutkovsky, V., Sukhanov, V., and Glumov, V. (2010b). Motion equations and control of a free-flying space manipulator in reconfiguration mode. *Automation and Remote Control*, **71** (1), pp. 70–86.

Rutkovsky, V., Sukhanov, V., and Glumov, V. (2010c). Some control problems of free-flying space manipulation robots. I, II. *Mechatronics, Automation, Control*, (10; 12), pp. 52–59; 54–65.

Rutkovsky, V., Sukhanov, V., and Glumov, V. (2011). *Multimode Free-flying Space Manipulator: Motion Equations, Control and Software*. Institute of Control Sciences, Russian Academy of Sciences, Moscow.

Rutkovsky, V., Sukhanov, V., and Glumov, V. (2013). Some issues of controlling the free-flying manipulative space robot. *Automation and Remote Control*, **74** (11), pp. 1820–1837.

Rutkovsky, V., Sukhanov, V., and Glumov, V. (2015). On a small free-flying space robot control task. *Mechatronics, Automation, Control*, **16** (3), pp. 159–166.

Schaub, H. and Junkins, J. (2009). *Analytical Mechanics of Space Systems*. AIAA, Reston.

Smirnov, E. et al. (1985). *Motion Control of Mechanical Systems*. Leningrad University Publisher, Leningrad.

Somov, S. (2017). Pulse-width control of electroreaction engines for a station-keeping of land-survey satellite on sun-synchronous orbit. *AIP Conf. Proc.*, **1798** (020151), pp. 1–7. doi:10.1063/1.4972743.

Somov, S., Butyrin, S., and Somov, Y. (2017). Pulse-width control of satellite during initial stop of its rotation and a station-keeping on sun-synchronous orbit. *MESA*, **8** (1), pp. 65–73.

Somov, S. and Somova, T. (2021). Analysis of dynamic characteristics of flywheel clusters in a spacecraft attitude control system. *Izvestia RAS SamSC*, **23** (6), pp. 110–125.

Somov, Y. (1996). Feedback linearization and VLF techniques on the synthesis of spacecraft's gyromoment attitude control systems. In *IEEE Intern. Conf. on Systems, Man and Cybernetics. Information Intelligence and Systems*, vol. 4, Beijing, pp. 2522–2527.

Somov, Y. (2016). Guidance, navigation and control of information satellites: Methods for modeling, synthesis and nonlinear analysis. *MESA*, **7** (2), pp. 223–248.

Somov, Y., Butyrin, S., and Somov, S. (2021a). Dynamics of an autonomous spacecraft control system at initial transition to a tracking mode. *Cybernetics and Physics*, **10** (3), pp. 185–190.

Somov, Y., Butyrin, S., Somov, S., and Somova, T. (2020). Nonlinear digital and pulse-width control at approaching a space robot with a geostationary satellite. *MESA*, **11** (4), pp. 993–1001.

Somov, Y., Butyrin, S., and Somova, T. (2022). A space robot control at approaching and inspecting a geostationary satellite state. *Cybernetics and Physics*, **11** (1), pp. 30–36.

Somov, Y., Butyrin, S., Somova, T., and Somov, S. (2021b). Health checking autonomous attitude control system of Earth-observing miniature satellite in initial orientation modes. *IEEE Journal on Miniaturization for Air and Space Systems*, **2** (2), pp. 51–58.

Somov, Y. et al. (2019). Control of robot-manipulator during its preparation and capture of a passive satellite. *MESA*, **10** (3), pp. 421–432.

Somov, Y. and Somova, T. (2022). Autonomous guidance and control of a geostationary satellite during long-term conservation. *MESA*, **13** (1), pp. 63–71.

Somova, T. (2016). Attitude guidance and control, simulation and animation of a land-survey mini-satellite motion. *Journal of Aeronautics and Space Technologies*, **9** (2), pp. 35–45.

SR (2022). *Spacecraft refuelers*. URL: https://dzen.ru/a/Yfuo2y6ZckX585-K.

SR (2024a). *Eternal life for satellites: in-orbit refueling will usher in a new era of space exploration*. URL: https:// www.securitylab.ru/news/547203.php.

SR (2024b). *Refueling in orbit: the key to new space*. URL: https://naked-science.ru/article/nakedscience/zapravka-na-orbite.

SR (2025). *China has performed the world's first satellite refueling in geostationary orbit*. URL: https://habr.com/ru/companie/ru_mts/articles/929768/.

Sukhanov, V., Rutkovsky, V., and Glumov, V. (2014). Determination of workspace and required initial position of free-flying space manipulator at target capture. *Automation and Remote Control*, **75** (11), pp. 2014–2022.

Sukhanov, V., Silaev, A., and Glumov, V. (2015). Dynamic equations of free-flying space robot for feedback control tasks. *Automation and Remote Control*, **76** (8), pp. 1446 –1454.

Testoyedov, N., Rayevsky, V., Somov, Y., Titov, G., and Yakimov, Y. (2017). Attitude and orbit control systems of Russian communication, navigation and geodesic satellites: History, present and future. *IFAC-PapersOnLine*, **50** (1), pp. 6422–6427.

Timofeev, A. and Shardyko, I. (2013). Problems of using anthropomorphic robots in space. *Robotics and Technical Cybernetics*, (1), pp. 37–41.

Vallado, D. (2013). *Fundamentals of Astrodynamics and Applications*. Microcosm Press, Hawthorne.

Wie, B. (2008). *Space Vehicle Dynamics and Control*. AIAA, Reston.

Zemlyakov, S., Rutkovsky, V., and Sukhanov, V. (2006). Some control problems on the robotized in-orbit assembly of large space structures. *Automation and Remote Control*, **67** (8), pp. 1215–1227.